ROYAL SOCIETY OF CHEMISTRY

PAPER

Check for updates

Osteoimmunity-regulating nanosilicate-reinforced hydrogels for enhancing osseointegration†

Yuanyuan Li,[abc] Guangmei Yang,[ab] Yuting Wang,[ab] Yahong Li,[ab] Shu Zhang,[ab] Ruyi Li,[ab] Linxin Yang,[ab] Jian Wang,[ab] Xibo Pei, [ID][ab] Qianbing Wan [ID] *[ab] and Junyu Chen*[ab]

Following the introduction of osteo-immunomodulation as a new and important strategy to enhance material osseointegration, achieving an appropriate immune response after biomaterial implantation has become a significant challenge for efficient bone repair. In this study, a nanosilicate-reinforced sodium alginate (SA) hydrogel was fabricated by introducing montmorillonite (MMT) nanoparticles. Meanwhile, an immunogenically bioactive agent, harmine (HM), was loaded and released to induce macrophage differentiation into the M2 type. The fabricated SA/MMT/HM (SMH) hydrogel exhibited improved mechanical stiffness and stability, which also efficiently promoted macrophage anti-inflammatory M2 phenotype polarization and enhanced the secretion of pro-tissue healing cytokines for inducing a favorable immunomodulatory microenvironment for the osteogenic differentiation of bone marrow stromal cells (BMSCs). Furthermore, a rat air-pouch model and a critical-size bone defect model were used and the results showed that the SMH hydrogel increased the proportion of M2 macrophages and markedly reduced local inflammation, while enhancing desirable new bone formation. Transcriptomic analysis revealed that the SMH hydrogel accelerated the M1-to-M2 transition of macrophages by inhibiting relevant inflammatory signaling pathways and activating the PI3K–AKT1 signaling pathway. Taken together, this high-intensity immunomodulatory hydrogel may be a promising biomaterial for bone regeneration and provide a valuable base and positive enlightenment for massive bone defect repair.

1. Introduction

Reconstruction of a critical bone defect resulting from trauma, tumor, or congenital deformity remains a major clinical challenge worldwide.[1] Tissue engineering technology based on bone replacement materials is a common method for solving this problem. With the emergence of the osteo-immunomodulation concept, the design strategy for bone substitutes has shifted from "immunosuppressive" materials to "immunomodulatory" materials.[2] Macrophages, as an important part of the immune system, play a leading role in the inflammatory immune response triggered at the initial stage after implantation of

materials. They have a high degree of plasticity.[3] Depending on the different stimuli of the external environment, these cells can differentiate into the classical activated M1 type, producing pro-inflammatory factors that lead to tissue damage or differentiating into the M2 type, which secretes pro-healing cytokines, coordinating tissue remodeling.[4] Therefore, timely regulation of the polarization of macrophages toward the M2 phenotype may help reduce biomaterial-mediated inflammation, create a favorable bone osteoimmune microenvironment, and pave the way for accelerating bone regeneration.

Previous research showed that cell behaviors (such as migration, proliferation, and differentiation) can be modulated through the microenvironmental cues presented by biomaterials.[5,6] Macrophage phenotypes can be regulated through biomaterial modification, including physical properties (*e.g.*, stiffness and porosity), chemical properties (*e.g.*, surface charge and hydrophilicity), and biological properties. At present, among many modification strategies, biological modification is one of the most widely used and effective strategies, which can be achieved by incorporating growth factors, immunoactive molecules, and metal ions, among others.[7] Harmine (HM), a natural tricyclic β-carboline alkaloid, has various pharmacological effects, including anti-cancer, anti-inflammatory, and anti-depressive effects.[8–10] In the bone metabolism field,

[a] *State Key Laboratory of Oral Diseases, National Clinical Research Center for Oral Diseases, Chengdu 610041, China. E-mail: junyuchen@scu.edu.cn, champion@scu.edu.cn*

[b] *Department of Prosthodontics, West China Hospital of Stomatology, Sichuan University, No. 14, Section 3, South Peoples Road, Chengdu 610041, China*

[c] *Department of Preventive Dentistry, Affiliated Stomatology Hospital of Guangzhou Medical University, Guangdong Engineering Research Center of Oral Restoration and Reconstruction, Guangzhou Key Laboratory of Basic and Applied Research of Oral Regenerative Medicine, Guangzhou, China*

† Electronic supplementary information (ESI) available. See DOI: https://doi.org/10.1039/d3tb01509b

This journal is © The Royal Society of Chemistry 2023

J. Mater. Chem. B, 2023, **11**, 9933–9949 | **9933**

previous reports have proved that HM can inhibit the formation of osteoclasts and promote osteogenesis by facilitating the formation of type H blood vessels (a distinct capillary subtype that couples angiogenesis and osteogenesis).[11] Recently, it has been demonstrated to regulate the differentiation of macrophages into M2 type and promote osteogenesis.[12] Therefore, HM was introduced in this study as an immune bioactive agent with excellent immune regulatory properties. However, the therapeutic use of HM is limited because of its poor water solubility, burst release, short life, and histotoxicity.[13] To solve these problems, it is necessary to find a strategy for reducing the harmful effects of HM while enhancing its immunomodulatory function by formulating drug delivery systems for sustained release.

Among the many drug delivery platforms, alginate stands out because of its versatile properties, such as low toxicity, biodegradability, low cost, and hydrophilicity.[14,15] In particular, scientific and technological advances have provided a new prospect for alginate hydrogels to expand their applications in bone regeneration because they are one of the most used and successful materials for bone tissue engineering and bioprinting.[16] Despite these advances, there are still some limitations with applying these hydrogels for load-bearing bone tissues because of their poor mechanical strength. To overcome this obstacle, scientists have proposed a two-dimensional nanosilicate, montmorillonite (MMT), to improve the stiffness of the hydrogel.[17] These nanoparticles not only have the ability to improve the mechanical properties of the hydrogel but also induce osteogenesis, directly affecting the effectiveness of the osteogenesis system.[18] The hydrogels added with MMT have been shown to enhance the osteogenic differentiation of mesenchymal stem cells (hMSCs) even in media free of differentiation factors, which may push regenerative therapies to a new level.[19] In addition, MMT is also commonly used as a drug delivery platform because of its electrostatic interactions with other molecules.[20,21]

In this context, we used alginate as the base material and synthesized MMT-reinforced alginate hydrogels for loading HM—SA/MMT/HM (SMH). We hypothesize that this hydrogel has favorable mechanical strength and plasticity for bone defect repair. The release of MMT can directly induce bone formation; meanwhile, the release of HM can stimulate macrophages toward the M2 phenotype and secrete osteoblast-related cytokines to promote bone formation indirectly, thus maximizing the material's osteoblastic induction potential (Scheme 1). Our work aims to construct an osteoimmunity-regulating hydrogel system and explore the immunomodulatory mechanisms of this hydrogel in depth through transcriptome sequencing. This may provide theoretical evidence for designing bone substitution materials that regulate immune responses precisely and accelerate bone defect repair.

2. Materials and methods

2.1. Materials

Sodium alginate (SA) and calcium chloride were purchased from Solarbio (China). Montmorillonite (MMT) and harmine (HM) were purchased from Aladdin Biochemical Technology

Co. Ltd. (Shanghai, China). Dulbecco's Modified Eagle's Medium (DMEM), α-minimum essential medium (α-MEM), fetal bovine serum (FBS), trypsin, penicillin/streptomycin (P/S), and phosphate-buffered saline (PBS) were obtained from Gibco (Gibco, Grand Island, NY).

2.2. Preparation of the hydrogels

Concerning the hydrogel, 300 mg of SA powder was dissolved in Milli-Q water to prepare a 3% (w/v) SA solution. To this solution, 100 mg of MMT was added, stirred for 5 min, and shaken at 1000 rpm for 2 h at 37 °C to obtain a yellowish homogeneous SM solution. Subsequently, the required amount of HM was added to the SM solution and stirred at 37 °C for 1 h to obtain a homogeneous solution. When the mixture was formed, 2% $CaCl_2$ was poured into the system. After incubation for 20 min, the compound was rinsed with PBS, and the hydrogels were formed (Table S1, ESI†).
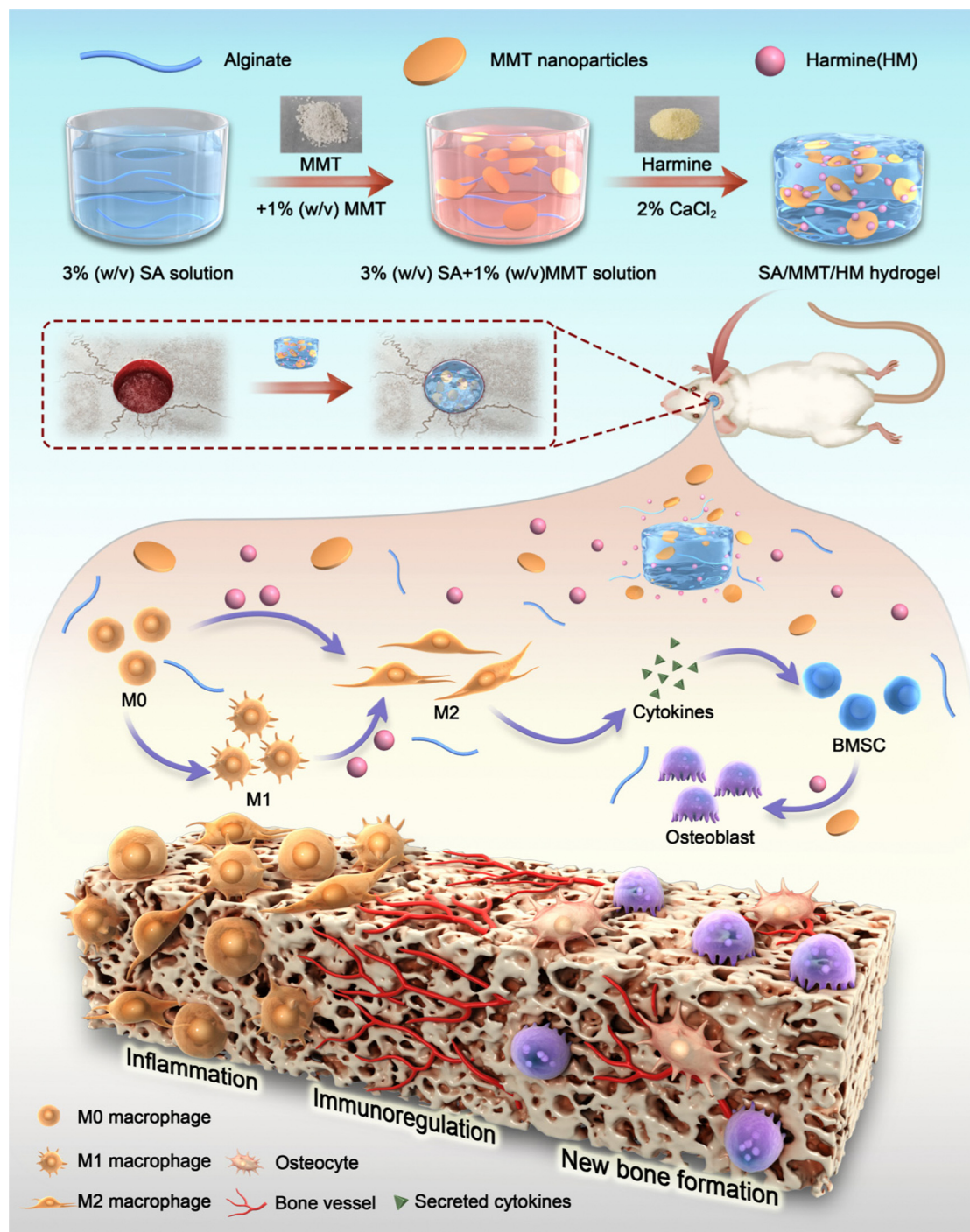
2.3. Characterization of SMH hydrogels

Cylindrical hydrogel samples were prepared using molds (1 × 5 cm) and then freeze–dried for 48 h. Subsequently, the morphology of the samples and lyophilized hydrogels was observed via scanning electron microscopy (SEM) (KYKY Technology Development Ltd., China) and transmission electron microscopy (TEM) (Tecnai G2 F20 S-TWIN, USA). A Thermo Gravimetric Analyzer (TGA; DSC1/1100LF, Switzerland) was used to record the thermal stability of each group of hydrogels. The test conditions were as follows: temperature rising from 100 °C to 800 °C at a rate of 10 °C min^{-1}, with N2 protection. Fourier-transform infrared spectroscopy (FTIR; Nicolet 6700, USA) analysis was performed to analyze the infrared absorption of the functional groups of SA, SM, and SMH. Energy-dispersive spectroscopy (EDS; KYKY, China) and elemental mapping were conducted via SEM, operating at 10 kV with a collection time of 40–55 s.

The compressive modulus of the hydrogels was measured with a universal testing machine (Instron 5567 USA). All the hydrogels were prepared in a cylindrical shape, measuring 12 mm in diameter and 5 mm in height, and tested after polymerization at a rate of 10 mm min^{-1}. The rheological properties of hydrogels were measured using an MCR 301 rheometer (Anton Paar, Austria), and the sample was prepared with a height of 1 mm and a diameter of 25 to fit the size of the rotor. The angular frequency varied from 0.1 to 100 rad s^{-1} at a strain rate of 0.5% to evaluate both the storage and loss modulus of hydrogels.

For the swelling ratio assay, after the dry weight of each sample (M0) was measured, the hydrogels were immersed in PBS (pH = 7.2) at 37 °C. At each designated time point, the hydrogels were removed, wiped with filter paper to remove any surface liquid, and weighed again (M1). The swelling ratio was calculated using the following equation: swelling ratio = (M1 − M0)/M0.

The HM released from hydrogels was measured as follows: 5 mL of gelled hydrogel was added to 150 mL of PBS and then placed in a shaking table (100 rpm) at 37 °C. At a specific time interval (1, 3, 6, 12, 24, and 48 h), 4.0 mL of supernatant was

9934 | *J. Mater. Chem. B*, 2023, **11**, 9933–9949

This journal is © The Royal Society of Chemistry 2023

Scheme 1 Schematic illustration of SA/MMT/HM hydrogel composites with immunomodulatory activity for enhanced bone regeneration. The HM released from the SA/MMT/HM hydrogel inhibited M1 macrophage polarization and activated M2 macrophages, inducing a favorable microenvironment for new bone formation. Abbreviation list: sodium alginate (SA); montmorillonite (MMT); Harmine (HM); and bone marrow stem cells (BMSCs).

collected for analysis and replaced with 4.0 mL of fresh PBS. The collected samples were centrifuged at 10 000 rpm for 15 min, and the supernatants were collected to determine HM concentration by UV-Vis spectrophotometry. Specifically, a series of HM (0–16 μg mL^{-1}) was dissolved in methanol to establish a standard curve. Then, the absorbance of the supernatant was recorded *via* a UV-Vis spectrophotometer and converted to concentration by the standard curve. The detection wavelength was 301 nm (Fig. S5, ESI†).

2.4. *In vitro* studies: preparation of hydrogel extracts

Hydrogels with diameters of 35 mm and heights of 1 mm were first immersed in 5 mL DMEM at 37 °C for 24 h. Subsequently, the supernatants were collected and filtered after centrifugation

This journal is © The Royal Society of Chemistry 2023

J. Mater. Chem. B, 2023, **11**, 9933–9949 | **9935**

at 4000 rpm for 15 min. Subsequently, 10% FBS and 1% P/S were added to the extracts and stored at 4 °C.

2.5. Cell culture

RAW264.7 cells were provided by the State Key Laboratory of Oral Diseases, Sichuan University (Chengdu, China). BMSCs were obtained from the bone marrow of femurs and tibias of 2-week-old rats as described in a previous study.[22] The BMSCs were cultured in 25 cm^2 flasks (Nest, USA) containing α-MEM supplemented with 10% FBS and 1% penicillin–streptomycin in a humidified atmosphere with 5% CO_2 at 37 °C.

2.6. Biocompatibility of SMH

Cell viability was investigated using a cell counting kit-8 (CCK-8) assay. Raw 264.7 cells (2.0×10^4 cells per well) were planted on 48-well plates and incubated overnight. Subsequently, the cells were treated with a blank control, SM, or SMH at various concentrations for 1, 2, and 3 days. After washing twice with PBS, the CCK-8 reagent was mixed with cell culture medium at a 1 : 10 ratio and added to each well. The plates were transferred to a dark environment at 37 °C for 2 h. Finally, the supernatant was transferred into a 96-well plate, and the absorbance was measured using a microplate reader (Thermo, USA) at 450 nm wavelength.

2.7. Macrophage polarization assay

Raw 264.7 cells were seeded in a 24-well plate at a density of 2×10^3 per well. Macrophages in the control group were cultured in regular medium at all times. The other three groups of macrophages were first treated with 100 ng mL^{-1} lipopolysaccharide (LPS, Sigma-Aldrich) for 6 h. Then, the media were replaced by regular medium, SM hydrogel extracts, and SMH hydrogel (8 μg mL^{-1}) extracts. After 24 h of cultivation, M1 and M2 macrophages were identified using immunofluorescence staining, qPCR, and ELISA.

2.7.1. Cell morphology. Different groups of cells were treated with the different methods mentioned above (Section 2.7). The cells were first fixed with 4% paraformaldehyde for 15 min and then permeabilized with 0.5% Triton X-100 for 5 min. Subsequently, F-actin and the nuclei were stained with tetramethylrhodamine (TRITC)-phalloidin (Solarbio, China) and DAPI, respectively. Finally, the cellular morphology was observed and captured using a Leica inverted fluorescence microscope (Leica DMi8, Germany).

2.7.2. Immunofluorescence analysis of macrophages. The expression of M1/M2 polarization markers in macrophages was evaluated by immunofluorescence analysis. The cells were fixed with 4% paraformaldehyde at normal temperature, followed by adding 10% FBS to block the nonspecific binding sites. The cells were then labeled with inducible nitric oxide synthase (iNOS, M1 marker) and arginase-1 (Arg-1, M2 marker; Abcam, UK).

2.7.3. Gene expression analysis by real-time polymerase chain reaction (RT-PCR). Total RNA was collected from cells using an RNA-quick purification kit (Yishan Biotech, Shanghai, China), following the manufacturer's procedure, and reverse-transcribed to cDNA using a Takara PrimeScritRT reagent Kit

(Osaka, Japan). RT-PCR was executed using a Power qPCR preMix system. The primer sequences used for this procedure are presented in the ESI† (Table S2).

2.7.4. Enzyme-linked immunosorbent assay (ELISA). To better understand the effect of hydrogels on inflammation, ELISA was performed to measure the levels of the relevant cytokines. The cell medium obtained from RAW 264.7 cells treated with different materials mentioned above was centrifuged at 4000 rpm for 20 min. The expression levels of TNF-α, IL-6, and IL-10 in the supernatant were measured using the corresponding commercial ELISA kits (Multi Sciences, China).

2.8. Preparation of conditioned medium (CM)

Raw264.7 cells were seeded in 6-well plates at a density of 1.0×10^5 cells per well. Macrophages in the control group were cultured in a regular medium at all time intervals. The other three groups of macrophages were first treated with LPS (100 ng mL^{-1}, 6 h) and then rinsed with PBS and incubated with the SM, SMH-l (4 μg mL^{-1}), and SMH-m (8 μg mL^{-1}) hydrogels. After 24 h, the supernatants from different groups were centrifuged and collected to obtain CM. Subsequently, the supernatants were mixed with osteogenic induction media containing 0.2 mM ascorbic acid, 10 mM β-glycerol phosphate, and 10^{-7} M dexamethasone at a 1 : 2 ratio.

2.9. *In vitro* osteogenesis-related research

BMSCs were seeded into a 24-well plate (5.0×10^4 cells) and cultured in α-MEM. After incubation for 24 h, the medium was replaced with osteogenic induction media obtained as described above for further incubation. After 7 or 14 days of osteogenic induction, the cells were fixed with 4% paraformaldehyde for 30 min and then stained with NBT/BCIP solution following the manufacturer's instructions (Beyotime Co., China). ALP activity assays were performed using an ALP activity kit (Beyotime Co., China). Alizarin Red S (ARS) staining was performed to observe the calcification nodules and investigate ECM mineralization. On day 14, the cells were fixed and stained with 1% Alizarin Red solution (Solarbio, China). For quantitative coloration of ARS, cetylpyridinium chloride (10%) was added to dissolve the Alizarin red stain, and the absorbance was measured at 542 nm using a microplate reader (Thermo, USA). All these staining images were observed under a stereomicroscope (Olympus, Japan).

The osteogenic gene expression of BMSCs was quantified *via* real-time quantitative polymerase chain reaction (RT-qPCR). On day 7, total cellular RNA was extracted using the RNA-Quick Purification kit (Yishan Biotechnology, China) and reversely transcribed to cDNA using a PrimeScript RT reagent kit (TakaRa, Japan). The expression levels of related genes (*Alp*, *Runx2*, *Osx*, *Ocn*, and *Opn*) were detected using SYBR Premix Ex TaqII (Takara, Japan). Primer sequences are listed in Table S2 (ESI†).

2.10. *In vivo* studies

2.10.1. Ethics statement. The 6-week-old Sprague–Dawley (SD) male rats were purchased from Dashuo Laboratory Animal Co., Ltd (Chengdu, China). Animal care and experiments were

9936 | *J. Mater. Chem. B*, 2023, **11**, 9933–9949

This journal is © The Royal Society of Chemistry 2023

performed according to the guidelines of the Institutional Animal Care and Use Committee of Sichuan University, Chengdu, China (WCHSIRB-D-2022–279).

2.10.2. Rat air-pouch model. The SD rats were assigned to three groups (black-control, SM, and SMH groups, n = 3). According to the report,[23] a dorsal air pouch was first developed on the rats' back by subcutaneously injecting 10 mL of sterile air. Three and six days later, 5 mL of sterile air was reinjected to maintain the air pouches. On day 7, the rats were anesthetized *via* an intraperitoneal injection of pentobarbital, and the skin around the air pouch was then shaved and sterilized. A 1 cm incision was made at the edge of the air pouch to insert the hydrogel (5 × 5 mm), and the incision was then closed.

2.10.3. Histological, immunohistochemical, and immuno-fluorescence analyses. Four days after material implantation, the rats were sacrificed. The skin covering the samples was harvested and fixed in 4% paraformaldehyde. Furthermore, tissue sections ($\approx$5 μm) were cut after embedding in paraffin. Subsequently, the sections were stained with hematoxylin and eosin (H&E) and Masson's trichrome stain to evaluate the collagen content and the thickness of the fibrous capsule. Immunofluorescence staining of CD68 (pan-macrophage marker; Abcam, UK) was performed to quantify the percentage of macrophages in the fibrous layer. In addition, immunohistochemical staining of CD86 (Abcam, UK) and CD206 (Abcam, UK) was performed to evaluate the different phenotypes of macrophages. The staining procedures were carried out according to the manufacturer's instructions.

2.10.4. Cranial defect model. The cranial defect model was established, as reported previously.[24] In brief, the rats were anesthetized with an intraperitoneal injection of pentobarbital followed by surgical site sterilization. Then, a longitudinal full-thickness incision of approximately 2 cm was made to expose the skull. One unilateral defect was created using a 5 mm-diameter trephine bur, and SA hydrogel, SM hydrogel, or SMH hydrogel (n = 3) was implanted. After implantation, the incisions were closed with surgical sutures, and the animals were sacrificed four weeks after surgery.

Blood samples were collected from the abdominal aorta for routine blood examinations and blood biochemistry assays, including red blood cell (RBC), white blood cell (WBC), alanine transferase (ALT), aspartate transferase (AST), creatinine (CREA), and urea (UREA) levels. Simultaneously, heart, liver, spleen, lung, and kidney specimens were collected for H&E staining.

2.10.5. Micro-CT analysis. The harvested samples were scanned using a micro-CT system (mCT-50, ScancoMedical Inc., Switzerland) to assess/detect new bone formation within the bone defect region. The scans were performed at 70 kVp, 114 μA, and a voxel size of 15 μm. Subsequently, Scanco medical visualizer software was used to reconstruct a three-dimensional (3D) model. The parameters including bone volume/total volume (BV/TV), trabecular number (Tb.N), trabecular separation/spacing (Tb.Sp), and trabecular thickness (Tb.Th) were calculated using an EV workplace.

2.10.6. Histological, immunohistochemical, and immuno-fluorescence analyses. For histological observation, all the

samples were decalcified for six weeks. Then, the decalcified calvarium was embedded and sectioned for H&E, Masson's trichrome, and Sirius Red staining to observe bone regeneration. In addition, immunohistochemical staining of Runx2 (Abcam, UK) and OCN (Abcam, UK) was performed. Finally, these images were scanned through flash digital microscopes (3D HISTECH Pannoramic250, Hungary) and assessed using Image J software with the IHC-Toolbox plugin (NIH, USA).

Immunofluorescence staining. Decalcified bone samples were sectioned at 100 μm thickness using a Leica CM3050 cryostat. The bone sections were air-dried for 15 min and hydrated with PBS for 5 min. After permeabilization for 10 min with 0.3% Triton X-100 and blocking in 5% donkey serum, the sections were incubated with diluted primary antibodies (1 : 150) against ALP, BMP-2, and OCN for 4 h at room temperature (RT). Then, the samples were rinsed with PBS five times and incubated with the corresponding secondary antibodies. Finally, images were captured under a confocal laser scanning microscope (Andor Dragonfly 200, Northern Ireland) and quantitatively analyzed using ImageJ software. All the antibodies are listed in Table S3 (ESI†).

2.11. Transcriptome sequencing of macrophages and bioinformatics analysis

The macrophages were treated with LPS (100 ng mL^{-1}, 6 h) first and then cultured with SM and SMH hydrogels as the control and experimental groups, respectively. Total RNA was extracted after 24 h using TRIzol, and cell lysates were stored at -80 °C for later sequencing. Transcription sequencing was performed using Illumina HiSeq X10 (Illumina, USA). The data were used for further analysis, and the read count value was obtained using bowtie2 and eXpress. The R package DESeq (1.30.0) was used to identify differentially expressed genes (DEGs). Two-fold changes with a P-value <0.05 were considered significant. A series of gene functional enrichment analyses, including GO and KEGG, were performed to evaluate the critical biological attributes.
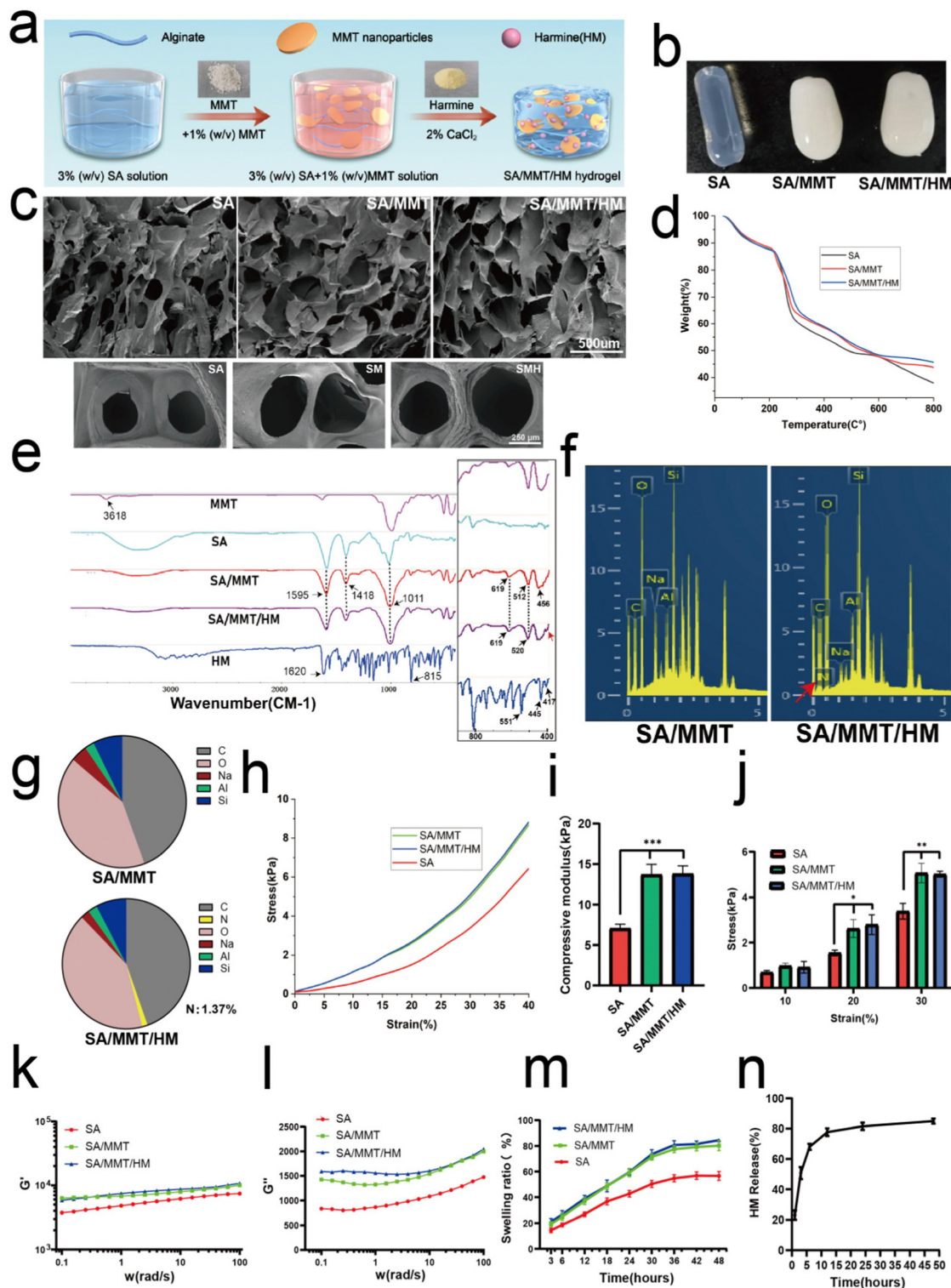
2.12. Statistical analysis

The results of the experiments are presented as means ± standard deviations (SD). Statistical analyses were performed using a two-tailed Student's t-test or one-way analysis of variance (ANOVA) combined with *post hoc* Tukey tests using GraphPad Prism 9, with $P < 0.05$ indicating statistical significance (*$P < 0.05$, **$P < 0.01$, ***$P < 0.001$, and ****$P < 0.0001$).

3. Results and discussion

3.1. Synthesis and characterization of SMH hydrogels

The simple mixing technique described previously was applied to fabricate the composite hydrogels comprising SA, MMT, and HM (Fig. 1a). The SEM images of MMT and HM are presented in Fig. S1 (ESI†). MMT was revealed as being a lamellar stacked structure with a particle size ranging from tens to hundreds of nanometers under a transmission electron microscope

This journal is © The Royal Society of Chemistry 2023

J. Mater. Chem. B, 2023, **11**, 9933–9949 | **9937**

Fig. 1 Preparation and characterization of SA/MMT/HM hydrogels. (a) Schematic illustration showing the fabrication process of the SA/MMT/HM hydrogel. (b) and (c) Digital photograph and SEM images of the hydrogel samples (scale bar: 500 μm, up; scale bar: 250 μm, down). (d) TGA curves of SA, SA/MMT, and SA/MMT/HM. (e) FTIR spectra of SA, MMT, HM, SA/MMT, and SA/MMT/HM. (f) EDS spectra of C, O, Na, Al, Si, and N for SA/MMT and SA/MMT/HM hydrogels. (g) The corresponding proportion of the element composition of each sample obtained from EDS. (h) and (i) Stress–strain curve and compression modulus of different hydrogels. (j) Instantaneous compressive stress of hydrogels at different strain levels. (k) and (l) Rheological analysis of different samples as a function of angular frequency. (k) Storage modulus (G'). (l) Loss modulus (G''). (m) Swelling ratios in the three groups of hydrogels. (n) Cumulative release (%) of drug from SA/MMT in PBS at pH = 7.2. Data are presented as mean ± SD ($n = 3$; *$P < 0.05$ and **$P < 0.01$, ***$P < 0.001$).

(Fig. S2, ESI†). When the hydrogels were formed, SA hydrogels were completely translucent, whereas SM and SMH hydrogels had some opacity because of the presence of MMT (Fig. 1b). The surface morphology of the lyophilized samples imaged by SEM confirmed a regular interconnected and ordered porous structure of the hydrogels. The pore size of the hydrogels was affected by the addition of MMT, with an average of 360.2 μm for SM hydrogels, which was larger than that of the SA hydrogels (257.4 μm) (Fig. 1c and Fig. S3, ESI†). This increase in the pore size of SM hydrogels can be attributed to the hydrophilicity of MMT. The layer structure of MMT promotes water absorption within the pores, leading to the generation of large pores.[25] However, there were no apparent differences in morphology between the SM and SMH groups, indicating that the incorporation of HM did not affect the microstructure of the hydrogels; a low dose of HM may explain this phenomenon.

Thermogravimetric analysis (TGA) of various samples indicated that the successful introduction of both MMT and HM could improve the thermal stability of hydrogels (Fig. 1d) as the residual masses of SA, SM, and SMH hydrogels at 800 °C were 37.98%, 43.80%, and 45.67%, respectively. The FTIR spectra (Fig. 1e) of SA showed a characteristic peak at 1595 cm^{-1}, which was assigned to C=O stretching vibrations, and a peak at 1418 cm^{-1} corresponding with COO$^-$ symmetric vibrations. The FTIR analyses of SM demonstrated the inclusion of MTT in the alginate matrix by the presence of specific peaks of MMT in the composite samples. Therefore, the peaks found at 1011 cm^{-1} corresponded with the Si–O–Si stretching vibrations, whereas the 456 cm^{-1} and 512 cm^{-1} corresponded with the Al–O–Si vibrations. On comparing the FTIR spectrum of SM and pure MMT, the Si–OH stretching of MMT at 3618 cm^{-1} disappeared in the spectra of SM, demonstrating that active sites of the polymer matrix interacted with MMT.[26] Meanwhile, the O–H (3000–3600 cm^{-1}) stretching of SA was suppressed in SM because hydrogen bonds formed between SA and MMT.[27,28] On comparing SM and SMH, the Al–O–Si stretching vibration at 512 cm^{-1} was shifted to 520 cm^{-1}, indicating that HM should have been successfully loaded in the SMH hydrogel. Also, the broad peak at 456 cm^{-1} in the SMH group (as indicated by the red arrow) might be correlated to the presence of HM. EDS analysis was performed, and C, O, Na, Al, and Si peaks were determined to evaluate the elemental composition of SM and SMH hydrogels (Fig. 1f). The intense peaks of C, O, and Na were characteristic of SA, whereas the peaks of Al and Si indicated the presence of MMT. The EDS spectrum confirmed that the characteristic elemental nitrogen (N) in HM was only observed in SMH, with none observed in SM (as indicated by the red arrow). In addition, the content of N existing in SMH was about 1.37 wt% (Fig. 1g). Additionally, the elemental maps showed that the Na, Al, Si, C, N, and O elements were evenly distributed in the SMH hydrogels, indicating the good dispersibility of MMT and HM in the hydrogels (Fig. S4, ESI†). In summary, a series of characterizations confirmed that the SMH composite hydrogel was synthesized successfully.

The incorporation of MMT into SA markedly improved the mechanical strength of the hydrogels, as demonstrated by compression and rheological tests (Fig. 1h–i). The representativ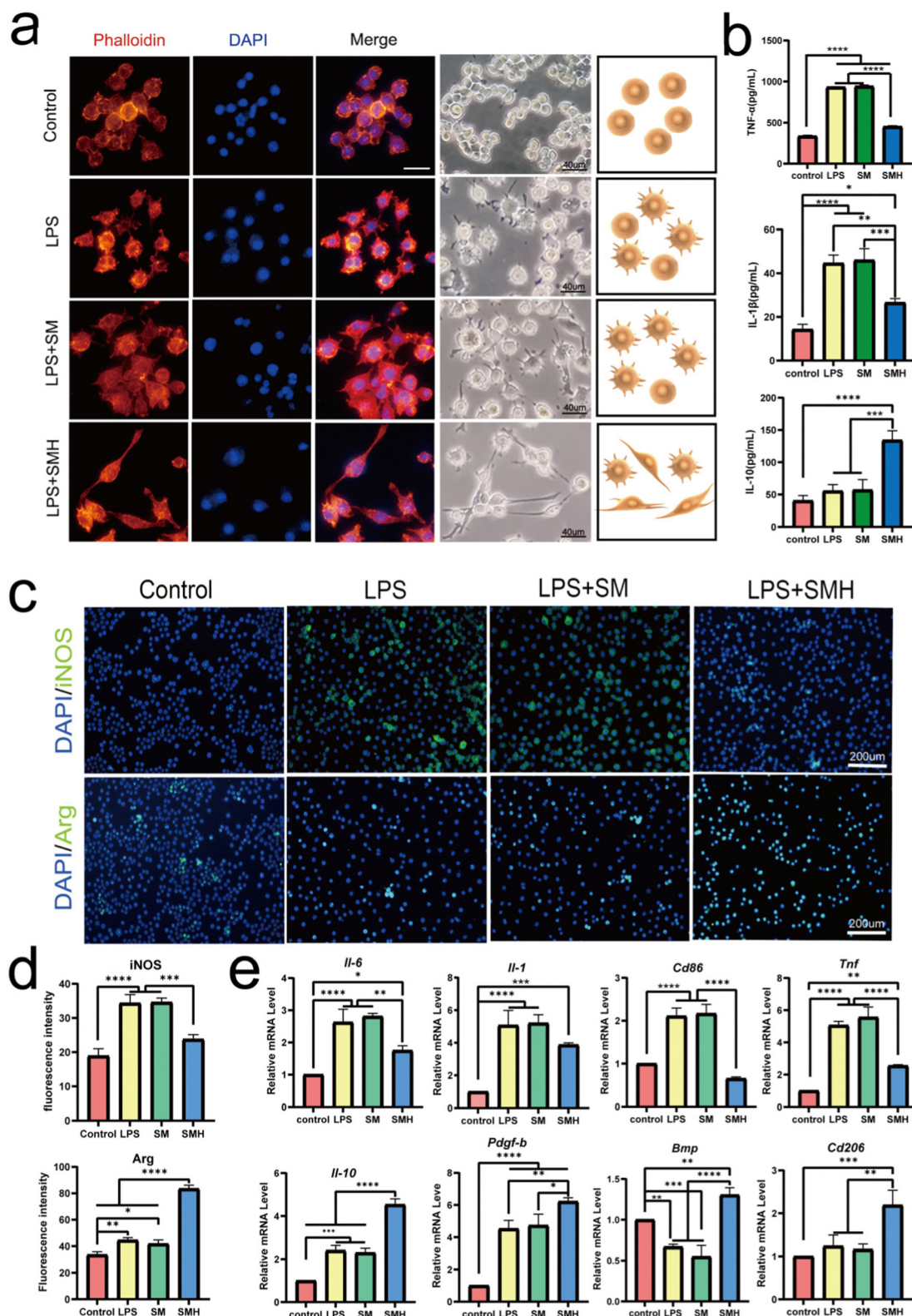e strain–stress curves for the three groups of hydrogels are presented in Fig. 1h. The results of compression modulus of SM and SMH hydrogels were similar, approximately 13.76 ± 4.13 kPa, which was significantly higher than that of the SA hydrogel, approximately 7.09 ± 1.99 kPa (Fig. 1i). Furthermore, SM and SMH hydrogels had significantly higher compressive strength at strain rates of 20% and 30% compared with the SA hydrogels (Fig. 1j), indicating that the hydrogels containing MMT nanoparticles had stronger mechanical properties than the pure SA hydrogel. Concerning the rheological properties of hydrogels, the storage modulus (G') of all hydrogels was higher than the loss modulus (G''), indicating their elastic nature (Fig. 1k and l). The frequency sweeps showed that the storage modulus (G') of the SM and SMH hydrogels was approximately 8.06 kPa, which was significantly higher than that of the SA hydrogels (5.52 kPa), suggesting a stiffer structural network formed in the SM nanocomposite hydrogels. The improvement in mechanical properties could provide the SMH hydrogel with increasing stability, and it could remain longer at the implanted site, which is beneficial to the formation of bone *in vivo*.

In addition, the swelling ratios of SM and SMH composite hydrogels were similar and significantly higher than that of the SA hydrogels because of the hydrophilic nature of MMT (Fig. 1m). This finding demonstrated the higher water absorption capacity of SMH hydrogels, which can facilitate the absorption of physiological fluids and the transfer of nutrients and metabolites through hydrogel scaffolds, ultimately promoting microvessel ingrowth and tissue regeneration. Moreover, the cumulative release trend of HM was consistent with previous literature.[29] HM was released quickly in the first 3 h, which endowed the drug carrier system with a rapid and efficient anti-inflammatory ability at the early stage. The release rate slowly decreased after 24 h. By the second day, the release rate of HM became stable (Fig. 1n).

3.2. SMH regulated macrophages to differentiate into the M2 phenotype

First, according to the previous cytotoxicity study of HM (Fig. S6, ESI†), composite hydrogels with different concentrations were prepared as carriers for the drug delivery system. The CCK8 assay results indicated that SMH-l and SMH-m hydrogels had no cytotoxicity toward RAW264.7 cells (Fig. S7, ESI†) and provided a comfortable living environment for the cells. In addition, PCR results showed that the SMH-m groups had the best anti-inflammatory effects (Fig. S8, ESI†). Thus, we considered the SMH-m group as the optimal concentration group and deemed it an experimental group for further studies.

Next, we explored the anti-inflammatory properties of SMH. The RAW264.7 cells were pre-cultured in a normal medium or LPS (100 ng mL^{-1}, for M1 polarization) and subsequently treated with the extracts of various hydrogels for 24 h. Meanwhile, we observed the change in the morphology of macrophages in response to different groups of hydrogels (Fig. 2a). In the control group without LPS, the majority of RAW264.7 cells appeared small and round, and after stimulation with SM, the cells mainly showed a fried egg shape, similar to that observed

Fig. 2 SA/MMT/HM promoted the polarization of macrophages from M1 to M2 phenotype *in vitro*. (a) Morphological analysis of RAW264.7 cells by fluorescence staining [DAPI (blue), TRITC-Phalloidin (red)] using a light microscope (scale bar: 40 μm). (b) Cytokine productions of TNF-α, IL-1β, and IL-10 secreted by macrophages determined using ELISA kits. (c) Immunofluorescence staining of macrophages: iNOS (M1 marker) and Arg-1 (M2 marker) are labeled in green (scale bar: 200 μm). (d) Corresponding iNOS and Arg-1 fluorescence intensity quantification. (e) The mRNA expression levels of factors associated with M1 polarization (*Il-6, Tnf-α, Il-1, Cd86*) and M2 polarization (*Il-10, Cd206, Pdfg-β, Bmp*) were detected by RT-PCR. All the statistical data are presented as mean ± SD ($n = 3$; *$P < 0.05$ and **$P < 0.01$, ***$P < 0.001$, ****$P < 0.0001$).

in the LPS group. However, the cells in the SMH group were prone to being long and spindle-shaped. It is believed that classical M1 macrophages are usually flat with multiple synaptic structures,[30] whereas M2 macrophages are long and spindle-shaped.[31–33] Changes in morphology suggested changes in macrophage phenotype and function.

iNOS is a classical marker for M1 macrophage polarization, whereas Arg-1 is a classical marker for M2 polarization.[34,35] Immunofluorescence assay revealed that the proportion of iNOS$^+$ M1 macrophages decreased 1.46 times in the SMH group, compared with the SM group. In contrast, the percentage of Arg-1$^+$ M2 macrophages increased about 1.98 times (Fig. 2c and d), further confirming that the switch from M1 to M2 polarization in macrophages was achieved after administering the SMH hydrogel.

Meanwhile, *Cd206*, *Il-10*, *Bmp*, *Pdgf-β*, and other anti-inflammatory and pro-healing genes were more highly expressed in the SMH group, suggesting a higher proportion of M2 macrophages. In contrast, the expression levels of M1-related genes, such as *Cd86*, *Inos*, *Tnf-α*, and *Il-6*, showed an opposite trend (Fig. 2e). Next, we detected the involved cytokines. Compared with the SM group, the SMH group showed a 2.35-fold increase in the concentrations of IL-10. In contrast, the concentrations of TNF-α and IL-1β decreased approximately 1.74-fold and 1.72-fold, respectively (Fig. 2b). All these data demonstrated that SMH could induce M2 polarization of macrophages, leading to the down-regulation of LPS-mediated pro-inflammatory cytokines. Changes in cytokine secretion may mediate the effect of macrophages on BMSCs, as IL-10 secreted by the M2 macrophages has been demonstrated to promote the osteogenic differentiation of BMSCs.[36]

It is worth mentioning that the SM hydrogel we prepared was more likely to induce M1 polarization of macrophages. This phenomenon was similar to the previous research,[37,38] probably ascribing to the lack of purification of SA, given that it has been reported that the effect of SA on macrophage activity differs depending on the degree of purification, the M/G ratio, and viscosity.[39,40] Our study indicated that loading HM may be a powerful method for regulating the macrophage response in SM-based hydrogels.

3.3. SMH triggered anti-inflammatory immunoregulation to promote osteogenesis

Next, to investigate the immunomodulatory effect of SMH hydrogel-activated macrophages toward BMSCs, a conditioned medium (CM) was prepared. The CM derived from the supernatant of macrophages cultured with control, SA, SM, and SMH hydrogels was collected and used to stimulate BMSCs (Fig. 3a). Considering that the immunomodulatory effect of SMH may be dose-dependent, we introduced SMH in two different concentrations (SMH-l and SMH-m) to increase the reliability and comparability of the experimental results.

After 7 or 14 days of osteogenic induction, ALP and ARS staining were performed to assess the osteogenic differentiation of BMSCs. As an indicator of the osteogenic capacity of BMSCs at the early stage, ALP was first detected by staining and quantitative determination. As shown in Fig. 3b and c, ALP

activity was the highest in the SMH-h group, followed by the SMH-l, control, and SM groups. Meanwhile, ARS staining revealed decreased mineralization in the SM group (Fig. 3d). An increased intensity of red color was observed in the SMH-m group, and quantity measurement indicated better mineralization in the SMH-m hydrogels than those in the SMH-l and SM hydrogels (Fig. 3e). The abovementioned experiments suggested that both the SMH-m and SMH-l groups promoted osteogenic differentiation of BMSCs. The SMH-m group exhibited a stronger effect than the SMH-l group, which may be because of the stronger immunomodulatory effect of the SMH-m group on macrophage polarization.
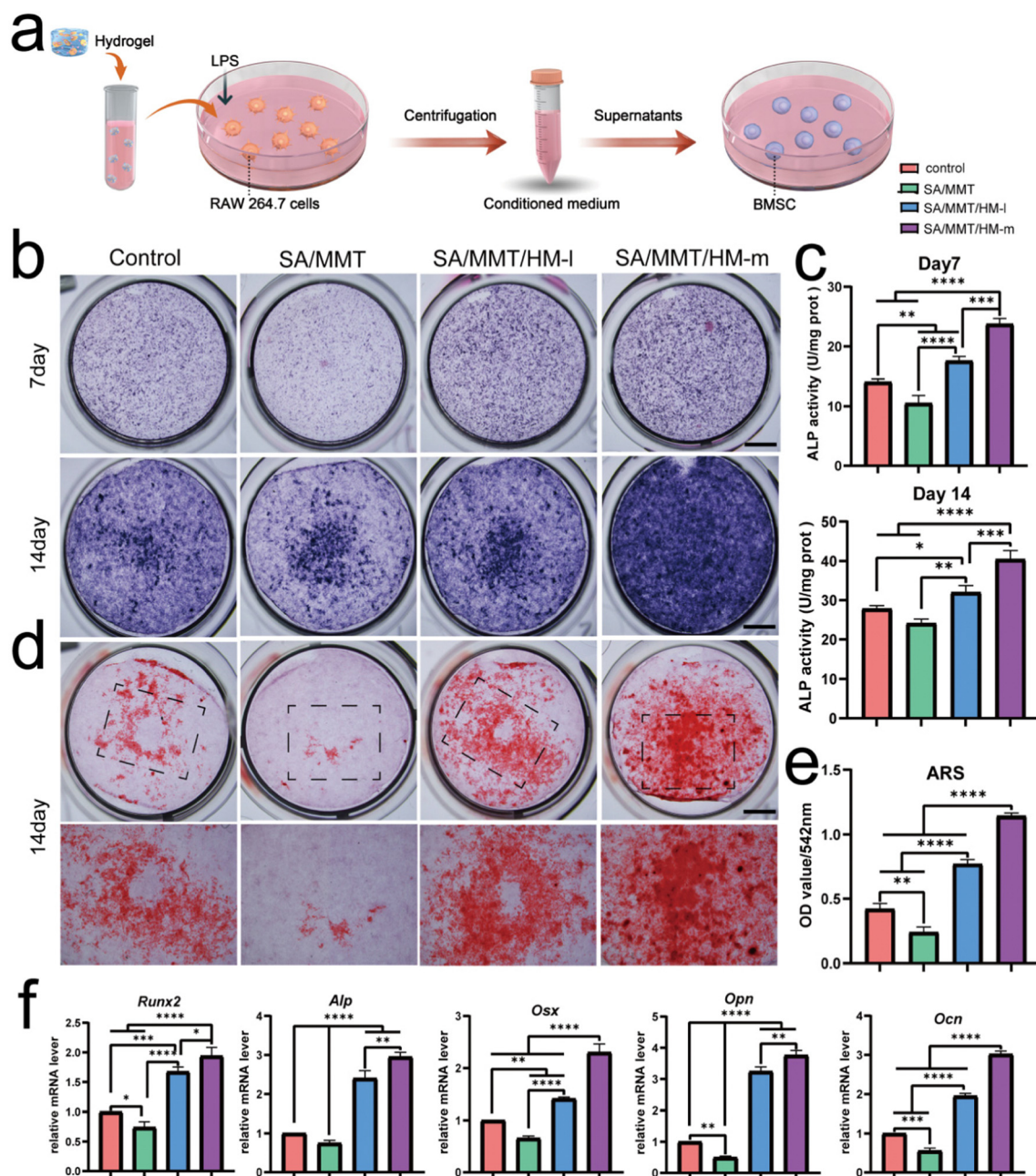
RT-PCR was performed to assess the impact of CM on osteogenic transcription factors, which showed a tendency similar to the staining results. BMSCs cultured with CM from the SMH-m group resulted in higher gene expressions of *Runx2*, *Alp*, *Opn*, *Ocn*, and *Osx*, indicating that SMH may be a promising biomaterial for facilitating osteogenesis. However, the SM group showed lower mRNA levels of these osteogenesis-related genes, possibly because of the absence of M2 macrophages in the SM group (Fig. 3f). In general, the CM derived from SMH demonstrated the best effects on osteogenic differentiation, indicating that the macrophages cultured with SMH-secreted cytokines were conducive to osteogenesis and exerted the strongest immunomodulatory effect. This also suggested that macrophage polarization is an attractive target to leverage for controlling inflammation and acquiring immune homeostasis for osteogenesis.

3.4. SMH regulated macrophage phenotypic alteration after implantation

Although inflammation plays a critical role in the initial phase of tissue healing after material implantation, excessive inflammatory responses usually hinder the tissue regeneration process, eventually resulting in premature absorption, rejection, and fibrosis of materials.[41] Activating the M1 phenotype of macrophages first and then guiding them to transform to the M2 phenotype at an appropriate time is the key to enhancing the effect of material osseointegration.

The inflammatory reaction triggered by SMH *in vivo* was measured by a rat air-pouch model. This model is widely used to study various inflammatory processes and has obvious advantages over other inflammatory models in the biochemical analysis of exudate and inflammatory cells and histological analysis of air-pouch lining.[42] The model forms a sterile subcutaneous cavity, which can be used to insert biomaterials and study the inflammatory response of materials. The local environment provided by the air pouch is conducive to the study of cell infiltration and the production of related inflammatory cytokines/chemokines.[43,44]

At the initial stage of material implantation, circulating monocytes could infiltrate the injured site and differentiate into macrophages, reaching a peak accumulation period around four days after operation.[45] Therefore, we performed histological examinations four days after sample implantation. H&E and Masson's trichrome staining showed a thinner fibrous layer in

This journal is © The Royal Society of Chemistry 2023
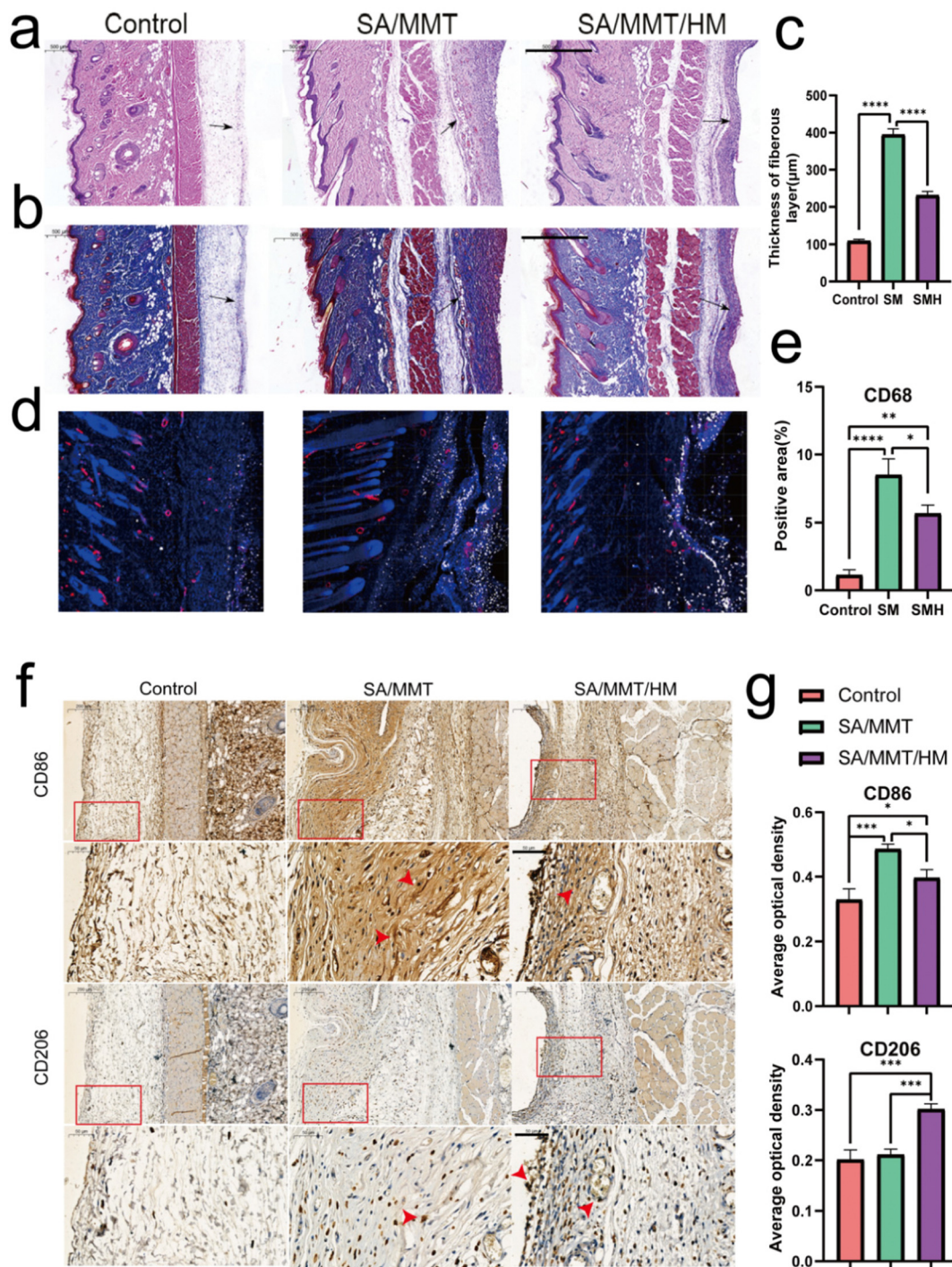
J. Mater. Chem. B, 2023, **11**, 9933–9949 | **9941**

Fig. 3 Osteogenic activities of BMSCs cultured with various conditioned media *in vitro*. (a) Schematic diagram. We used the supernatants of RAW264.7 cells treated with different hydrogel extracts as a conditioned medium to assess the macrophage polarization effect on BMSC osteogenesis. (b) ALP staining of BMSCs from each group after 7 and 14 days of osteoinduction. (c) Quantitative analysis of ALP activity. (d) ARS staining images as observed under a microscope on day 14 (scale bar: 2 mm). (e) Quantitative analysis of ARS staining. (f) RT-PCR results of selected osteogenic markers in BMSCs cultured for 14 days. All statistical data are presented as mean $\pm$ SD ($n = 3$; *$P < 0.05$ and **$P < 0.01$, ***$P < 0.001$, ****$P < 0.0001$).

SMH groups compared with SM groups, suggesting a mild inflammatory response (Fig. 4a–c). When hydrogels were implanted into the air pouches, the inflammatory reaction was triggered, and macrophages were one of the first responding cells gathering around the implants. Immunofluorescence staining results of CD68 (an important marker of macrophages in rats) showed numerous macrophages around hydrogels in each implantation group. Furthermore, the number of infiltrated macrophages was remarkably reduced in the SMH group

compared with that in the SM group (Fig. 4d and e), indicating inflammation resolution.

To further verify the M2 regulatory role *in vivo*, immunohistochemical staining was performed to assess the effect of the SMH composite hydrogel on macrophage polarization. Compared with the SM group, the SMH group had lower expressions of CD86 (M1 macrophages). However, CD206 (M2 macrophages) staining of fibrous layers revealed a higher number of M2 macrophages in the SMH group compared with the SM group

Fig. 4 Results of rat air-pouch model. (a) and (b) H&E staining and Masson's trichrome staining of the skin from the air pouch. The black arrows represent fibrous layers (scale bar: 500 μm). (c) Fibrous layer thickness of air pouch skin. (d) Immunofluorescence images of CD68 (white), α-SMA (red), and cell nucleus (blue) stained at four days. (e) Semi-quantitative analysis of immunofluorescence staining. (f) Immunohistochemical staining of macrophage surface markers, including CD86 and CD206, four days after implantation. The lower panels presented higher magnifications in the areas within the red rectangles in the upper panels. Red arrows indicate the positive staining area (scale bar: 50 μm). (g) Quantitative analysis of the corresponding immunohistochemical staining ($n = 3$). All the statistical data are presented as mean ± SD ($n = 3$; *$P < 0.05$ and **$P < 0.01$, ***$P < 0.001$, ****$P < 0.0001$).

(Fig. 4f and g), which may account for milder inflammation in the SMH group.

Biomaterials implanted in the body activate the immune system and trigger a foreign body response (FBR).[46] Well-designed biomaterials should activate macrophages into a desired phenotype, leading to timely resolution of FBR. The *in vivo* rat air-pouch model data were consistent with the *in vitro* results, demonstrating favorable immunomodulation properties of the

This journal is © The Royal Society of Chemistry 2023

J. Mater. Chem. B, 2023, **11**, 9933–9949 | **9943**

SMH hydrogel, which could induce M1 macrophages recruited by the SM hydrogel to transform into the M2 phenotype and create a preferable ratio of M1/M2. Thus, treatment with SMH hydrogels led to a pro-healing environment and promoted subsequent osteogenic differentiation.

3.5. SMH hydrogels for repairing bone defects in rats

Bone regeneration involves different cells (immune, progenitor, and mesenchymal cells) and subsequent signaling molecules (*e.g.*, chemokines, cytokines, and growth factors). Different numbers of immune cells with different functions enter the injury site, and the subsequently generated cytokines form a unique immune microenvironment. The level of bone repair is controlled by the upstream immune microenvironment to some extent.

The aforementioned findings demonstrate that SMH hydrogels formed an anti-inflammatory environment, accelerating tissue healing. To verify the role of the SMH composite hydrogels in inducing new bone formation *in vivo*, we constructed conventional rat skull defect models (Fig. 5a). We first evaluated the biocompatibility of the composite hydrogels *in vivo* by observing histological changes in major organs and the blood routine and biochemical indicators. After applying the material at the wound site for four weeks, all the rats were sacrificed, and organ samples were collected for H&E staining. There was no apparent toxicity or damage in the SM and SMH groups when compared with the normal SD rats (Fig. S9a, ESI†). Moreover, the blood routine and biochemistry indicators were in the normal range and showed no significant differences between groups (Fig. S9b, ESI†). These findings adequately demonstrate the excellent biosafety of SMH *in vivo*. However, the specific degradation product of this nanosilicate-reinforced alginate composite has not been thoroughly elucidated to date, and requires further investigation in future studies.

Four weeks after the operation, cranial samples were collected for micro-CT to assess the extent of bone healing. Almost no bone was newly formed in the control group; a small fraction of newly formed bone was detected at the bone margin in the SM group, indicating the limited osteogenic potential of SM hydrogels to promote bone healing. However, a large area of defect was covered by new bone in the SMH group (Fig. 5b). Quantitative micro-CT results further confirmed these observations. Based on quantitative analysis, the values of three indices reflecting new bone formation (BV/TV, Tb.N, and Tb.Th) in the SMH group were higher than those in the other two groups. In contrast, the value of Tb.Sp, which is negatively correlated with bone regeneration, decreased markedly in the SMH group (Fig. 5c).

H&E staining determined the inflammatory response and new bone formation. All the groups exhibited a low inflammatory response at the defect site. There was minimal new bone formation in the control group and a significant increase in the new bone tissue content in the SMH groups four weeks after implantation at the defect site (Fig. 5d). Masson's trichrome staining, as a staining method specific for collagen fibers, was also employed to further investigate the bone repair capability of the composite hydrogel. In the SM group, only a small fraction of bone was formed. In contrast, in the SMH group, denser collagen deposition was observed, indicating that the SMH hydrogel evoked a large amount of mature and mineralized bone formation (Fig. 5e). Sirius Red staining exhibited similar results, and more mineralized collagen fibers stained with light red color were observed in the defect areas in the SMH group (Fig. 5f). Immunohistochemical staining was performed to determine the expression of related proteins that played an important role in the early and late stages of osteogenesis. The expression levels of Runx2 and OCN were the highest in the SMH group compared to the other two groups (Fig. 5g and h). All these findings confirm that the SMH hydrogel has the strongest potential for bone repair, possibly because of the release of the anti-inflammatory drugs in the surrounding tissue, allowing for healthier bone growth. Immunofluorescence staining also confirmed that osteogenic markers, including ALP, BMP-2, and OCN, were up-regulated in the SMH group (Fig. 6 and Fig. S10, ESI†). The high expression of these molecules related to bone matrix formation and mineralization suggests that SMH can promote the osteogenic differentiation of BMSCs and accelerate bone repair in bone defect areas.
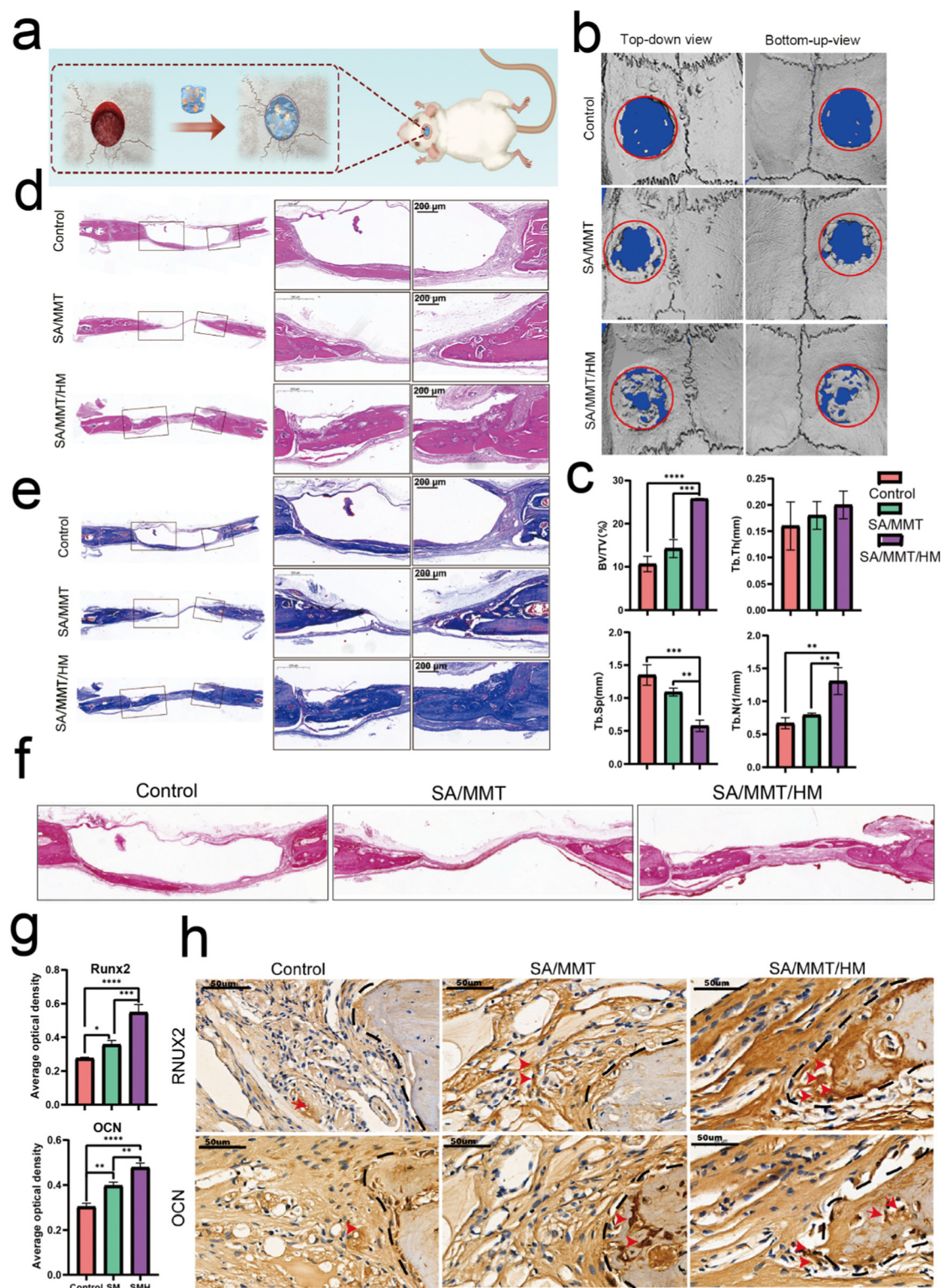
Mesenchymal stem cells are not simple repair cells but have multidirectional differentiation potential (repair, inflammatory, and immune regulatory cells). Their function depends on the regulation of the upstream immune microenvironment.[47] Therefore, to control the superior immune microenvironment, it is essential to channel BMSCs in the direction of repair and not to the other extreme. Our findings indicated a more favorable environment for osteogenesis when the immunomodulatory molecule HM was incorporated into the hydrogel. *In vivo* results were consistent with the *in vitro* osteogenic differentiation results and proved the effectiveness of SMH composite hydrogels in supporting new bone formation.

In brief, our study successfully developed SMH with excellent osteoimmunity-regulating properties, regulating macrophage M2 phenotype polarization and avoiding the adverse effects of the inflammatory storm during the initial period of material implantation. All these factors are beneficial for effective bone regeneration. All these findings confirmed that targeted regulation of macrophage-mediated bone immune microenvironments can improve the effect of bone replacement materials on tissue reconstruction.

3.6. Uncovering the underlying immunomodulatory mechanisms of SMH

Transcriptome sequencing was further used to analyze the potential mechanisms underlying SMH-induced M2 macrophage polarization. First, Pearson's correlation between samples was used to evaluate the stability of samples. Most of the correlation coefficients were within the acceptable range, indicating good clustering (Fig. 7a). The volcano map analysis of DEGs showed that 203 and 590 genes were up-regulated and down-regulated, respectively, in the SMH group compared with the control group (Fig. 7b).

Subsequently, GO analysis of DEGs was performed to reveal the SMH-activated cell function. All the DEGs are generally

9944 | *J. Mater. Chem. B*, 2023, **11**, 9933–9949

This journal is © The Royal Society of Chemistry 2023

Fig. 5 Evaluation of the osteogenic activity of SA/MMT/HM hydrogel *in vivo*. (a) Schematic illustration of implantation surgery. (b) 3D micro-CT reconstructions of the defects four weeks after surgery. (c) Quantitative analysis of the newly formed bone, including Tb.N, Tb.Th, Tb.Sp, and BV/TV. (d) and (e) H&E staining and Masson's trichrome staining images indicating the formation of the new bone. The images on the right show the higher magnifications of the areas within black rectangles in the images on the left (scale bar: 200 μm). (f) Sirius Red staining of areas with defects. (g) Quantitative analysis of immunohistochemical staining ($n = 3$). (h) Immunohistochemical staining of Runx2 and OCN four weeks after implantation (scale bar: 50 μm). Red arrows indicate the positive staining area. All the statistical data are presented as mean ± SD ($n = 3$; *$P < 0.05$ and **$P < 0.01$, ***$P < 0.001$, ****$P < 0.0001$).

This journal is © The Royal Society of Chemistry 2023
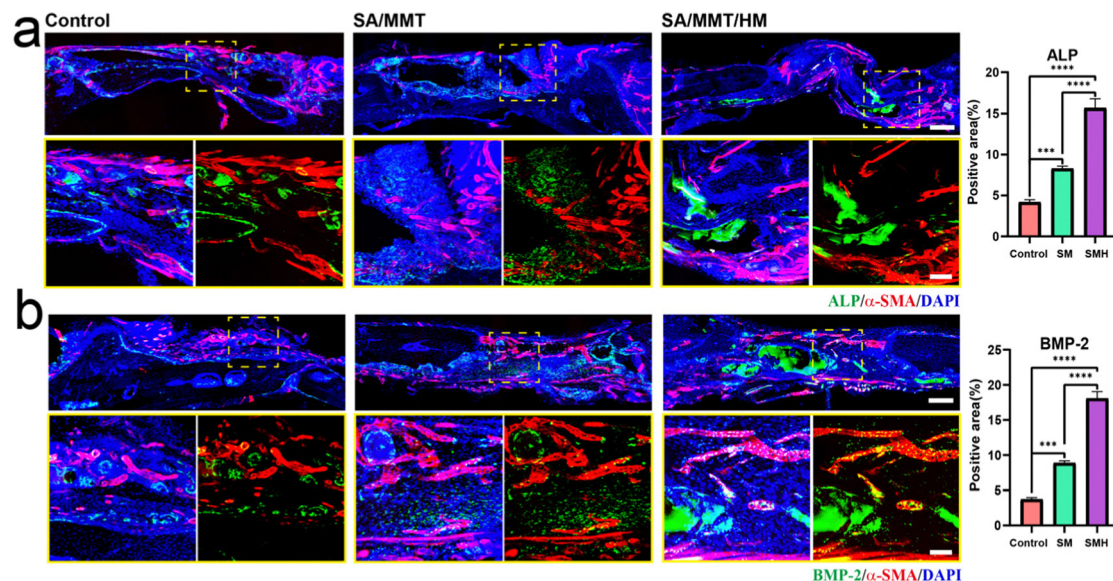
J. Mater. Chem. B, 2023, **11**, 9933–9949 | **9945**

Fig. 6 Immunofluorescence staining of cranial defect sections with ALP (a), BMP-2 (b), and α-SMA, and corresponding quantitative analysis of immunofluorescence staining results. Red (α-SMA), green (ALP, BMP-2), and blue (DAPI) (scale bar: 200 μm, up; scale bar: 50 μm, down).

grouped into three typical categories, including biological process (BP), molecular function (MF), and cell component (CC). Fig. 7c and d show the top 10 down/up-regulated enriched terms in the SMH group. We noted that most down-regulated biological processes were associated with immunity and inflammation-related responses, significantly impacting osteogenesis, consistent with the superior anti-inflammatory effect of SMH observed in the rat air-pouch model. Moreover, the significantly up-regulated genes were rich in regulating cell projection organization and signal transduction, which might correlate with the morphological changes in macrophages induced by SMH observed *in vitro*. In addition, the categories related to the chemical stimulus response were highly enriched, which might be caused by HM released from the hydrogel to stimulate macrophage polarization.

KEGG enrichment analysis (Fig. 7e) showed that after treatment with SMH hydrogels, the inflammatory signaling pathways, including Jak-STAT, Toll-like receptor, TNF, and NOD-like receptor signaling pathway, were down-regulated, which might help avoid the adverse effects caused by excessive inflammation. In contrast, cell adhesion molecules (CAMs) and the PI3k-Akt1 signaling pathway were up-regulated following SMH treatment, which is closely associated with M2 macrophage phenotypic transformation.[48,49] Subsequently, the differential gene expression related to the two forms of macrophages was further analyzed. The M1-related genes (*Il-1β*, *Tnf-α*, and *Il-6*) were down-regulated, whereas the M2-related genes (*Il-4*, *Il-10*, and *Arg-2*) showed an opposite trend. Moreover, the expression of some osteogenesis-related genes, such as *Pdgf-β*, *Tgf-β*, and *Bmp-6*, was enhanced when the cells were cultured with SMH (Fig. 7f). PDGF-β participates in angiogenesis during bone repair, promoting endothelial cell anastomosis and mediating the interactions between endothelial cells and pericytes.[50,51] TGF-β and BMP are indispensable for adequate mineralization
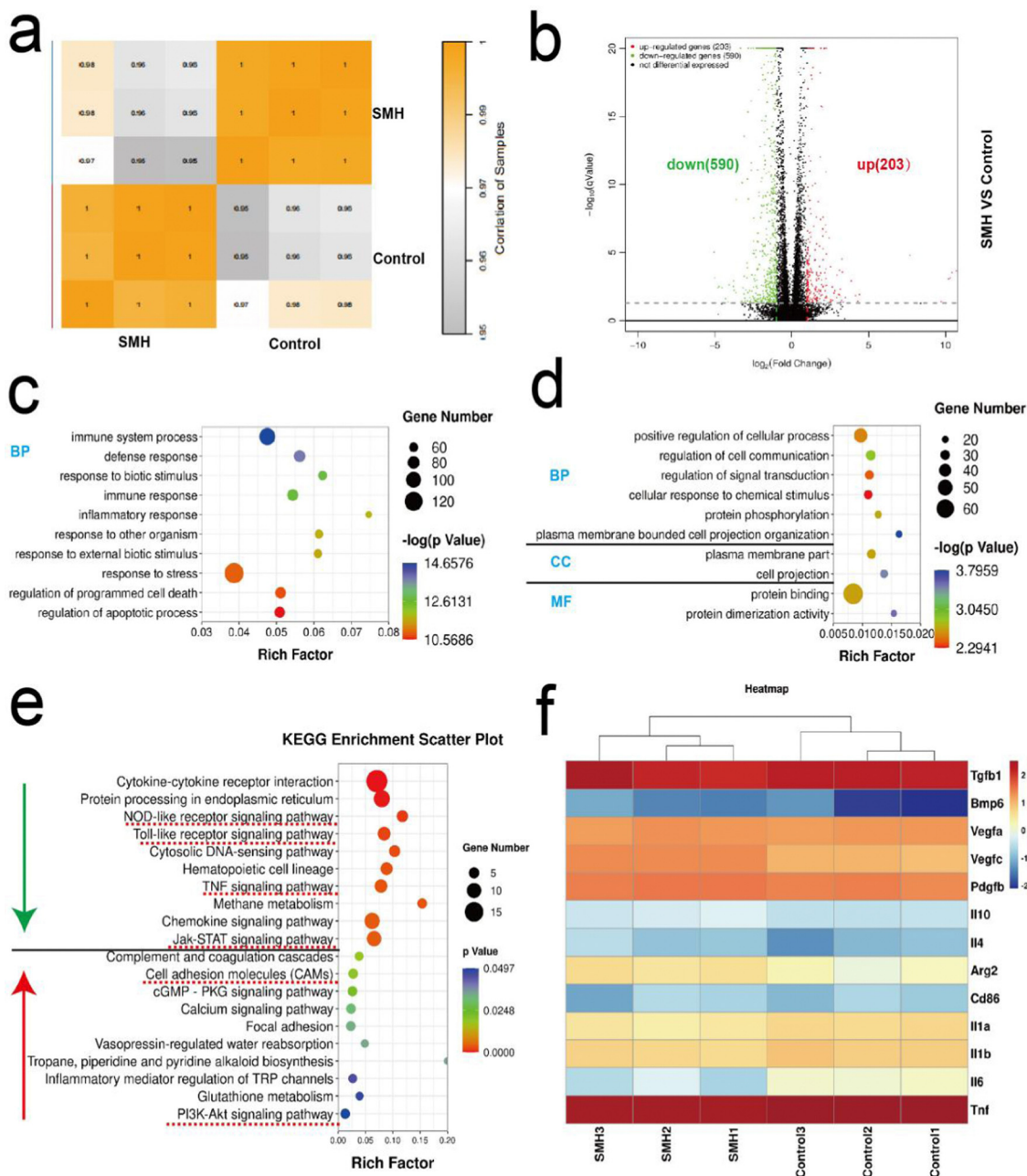
of osteoblasts, as TGF-β is an upstream protein of BMP signaling and BMP is a well-known osteogenic protein.[52,53] The genes with the largest variation were screened for a PCR assay, yielding comparable findings (Fig. S11, ESI†). The bioinformatic analysis results suggested that SMH can induce a change in the gene expression profile of macrophages to the M2 phenotype while promoting the secretion of a series of cytokines. Thus, the immune microenvironment was effectively regulated, and osteogenesis was boosted.

In summary, our study highlights the feasibility and importance of modulating inflammation levels by optimizing the properties of biomaterials. The developed SMH composite hydrogel improved the mechanical strength and stability and induced a favorable osteo-immune microenvironment by regulating the phenotypic switch of macrophages and secreting cytokines. The strong paracrine effects from the immune system could effectively regulate the behavior of osteogenesis-related cells, such as recruitment, proliferation, and differentiation, ultimately accelerating the bone tissue repair process. Our findings may provide a new strategy for applying HM as a novel immunomodulatory agent to reduce the inflammatory response caused by material implantation and promote bone regeneration. Furthermore, our findings provide a reference for designing and fabricating biomaterials combining the immunomodulatory property and osteogenic ability.

4. Conclusions

In conclusion, an appropriate immune response after biomaterial implantation is essential for bone tissue regeneration. In this study, SMH hydrogels with both superior mechanical strength and immunomodulatory performance for bone defect repair were successfully prepared. *In vitro* and *in vivo* findings

Fig. 7 Bioinformatic analysis of macrophage polarization induced by SA/MMT/HM hydrogel. (a) Heatmap of Pearson's correlation between samples (SM *vs.* SMH). (b) Volcano plot of differentially expressed genes (DEGs) of macrophages from different groups (SM *vs.* SMH). (c) Top 10 down-regulated terms from Gene ontology (GO) analysis ($n = 3$, P-value <0.05). (d) Top 10 up-regulated terms from GO analysis ($n = 3$, P-value <0.05) (BP, biological processes; CC, cellular components; MF, molecular functions). (e) Representative top 10 up-regulated and down-regulated pathways from KEGG analysis. (f) Heatmap analysis of DEGs involved in macrophage polarization.

showed that the composite hydrogel had improved mechanical properties and stability and reduced host inflammatory responses. Furthermore, transcriptome sequencing analysis showed that the hydrogel activated M2 macrophages through the PI3k-Akt signaling pathway and then up-regulated the expression of anti-inflammatory cytokines, inducing a favorable immunomodulatory microenvironment and promoting late osteogenesis. To the best of our knowledge, this is the first SM-based hydrogel developed with immunomodulatory properties for bone tissue engineering, and

the physicochemical properties and biological activities of this compound were investigated. In addition to the recognized osteoblastic activity of MMT, we found that SMH hydrogels mixed with HM could regulate macrophage phenotypes. This provides an effective strategy for promoting the application of SM in bone tissue regeneration. Biocompatible and bioactive nanocomposite hydrogels have excellent prospects in bone tissue engineering. Furthermore, they significantly promote bone regeneration and provide a valuable basis and positive enlightenment for large-scale bone defect repair.

Conflicts of interest

The authors declare no conflicts of interest.

Acknowledgements

References

1 A. J. Salgado, O. P. Coutinho and R. L. Reis, *Macromol. Biosci.*, 2004, **4**, 743–765.

2 D. P. Vasconcelos, A. P. Aguas, M. A. Barbosa, P. Pelegrin and J. N. Barbosa, *Acta Biomater.*, 2019, **83**, 1–12.

3 K. L. Spiller and T. J. Koh, *Adv. Drug Delivery Rev.*, 2017, **122**, 74–83.

4 Z. Chen, T. Klein, R. Z. Murray, R. Crawford, J. Chang, C. Wu and Y. Xiao, *Mater. Today*, 2016, **19**, 304–321.

5 P. Feng, Y. Kong, L. Yu, Y. Li, C. D. Gao, S. P. Peng, H. Pan, Z. Y. Zhao and C. J. Shuai, *Appl. Mater. Today*, 2019, **17**, 216–226.

6 C. J. Shuai, W. J. Yang, P. Feng, S. P. Peng and H. Pan, *Bioact. Mater.*, 2021, **6**, 490–502.

7 W. Bu, Y. Wu, A. M. Ghaemmaghami, H. Sun and A. Mata, *Regener. Biomater.*, 2022, **9**, rbac009.

8 J. Boni, C. Rubio-Perez, N. Lopez-Bigas, C. Fillat and S. de la Luna, *Cancers*, 2020, **12**, 2106.

9 X. Liu, M. Li, S. Tan, C. Wang, S. Fan and C. Huang, *Biochem. Biophys. Res. Commun.*, 2017, **489**, 332–338.

10 F. Liu, J. Wu, Y. Gong, P. Wang, L. Zhu, L. Tong, X. Chen, Y. Ling and C. Huang, *Prog. Neuro-Psychopharmacol. Biol. Psychiatry*, 2017, **79**, 258–267.

11 J. Huang, H. Yin, S.-S. Rao, P.-L. Xie, X. Cao, T. Rao, S.-Y. Liu, Z.-X. Wang, J. Cao, Y. Hu, Y. Zhang, J. Luo, Y.-J. Tan, Z.-Z. Liu, B. Wu, X.-K. Hu, T.-H. Chen, C.-Y. Chen and H. Xie, *Theranostics*, 2018, **8**, 2435–2446.

12 L. Wang, Q. Wang, W. Wang, G. Ge, N. Xu, D. Zheng, S. Jiang, G. Zhao, Y. Xu, Y. Wang, R. Zhu and D. Geng, *Front. Immunol.*, 2021, **12**, 657687.

13 L. Zhang, D. Li and S. Yu, *Arch. Pharmacal Res.*, 2020, **43**, 1259–1275.

14 A. C. Hernandez-Gonzalez, L. Tellez-Jurado and L. M. Rodriguez-Lorenzo, *Carbohydr. Polym.*, 2020, **229**, 115514.

15 H. H. Tonnesen and J. Karlsen, *Drug Dev. Ind. Pharm.*, 2002, **28**, 621–630.

16 R. Sheng, J. Chen, H. Wang, Y. Luo, J. Liu, Z. Chen, Q. Mo, J. Chi, C. Ling, X. Tan, Q. Yao and W. Zhang, *Adv. Healthcare Mater.*, 2022, **11**, 2200602.

17 R. Leu Alexa, R. Ianchis, D. Savu, M. Temelie, B. Trica, A. Serafim, G. M. Vlasceanu, E. Alexandrescu, S. Preda and H. Iovu, *Gels*, 2021, 7, 211.

18 A. K. Gaharwar, L. M. Cross, C. W. Peak, K. Gold, J. K. Carrow, A. Brokesh and K. A. Singh, *Adv. Mater.*, 2019, **31**, 1900332.

19 I. Erezuma, I. Lukin, C. Pimenta-Lopes, F. Ventura, P. Garcia-Garcia, R. Reyes, M. R. Arnau, A. Delgado, N. Taebnia, F. B. Kadumudi, A. Dolatshahi-Pirouz and G. Orive, *Int. J. Pharm.*, 2022, **623**, 121895.

20 I. Erezuma, T. Eufrasio-da-Silva, N. Golafshan, K. Deo, Y. K. Mishra, M. Castilho, A. K. Gaharwar, S. Leeuwenburgh, A. Dolatshahi-Pirouz and G. Orive, *Adv. Healthcare Mater.*, 2021, **10**, 2100217.

21 N. Khatoon, M. Q. Chu and C. H. Zhou, *J. Mater. Chem. B*, 2020, **8**, 7335–7351.

22 X. Gao, Y. Xue, Z. Zhu, J. Chen, Y. Liu, X. Cheng, X. Zhang, J. Wang, X. Pei and Q. Wan, *ACS Appl. Mater. Interfaces*, 2021, **13**, 97–111.

23 L. Fan, P. Guan, C. Xiao, H. Wen, Q. Wang, C. Liu, Y. Luo, L. Ma, G. Tan, P. Yu, L. Zhou and C. Ning, *Bioact. Mater.*, 2021, **6**, 2754–2766.

24 Y. Liu, Z. Zhu, X. Pei, X. Zhang, X. Cheng, S. Hu, X. Gao, J. Wang, J. Chen and Q. Wan, *ACS Appl. Mater. Interfaces*, 2020, **12**, 36978–36995.

25 M. Mehrali, A. Thakur, C. P. Pennisi, S. Talebian, A. Arpanaei, M. Nikkhah and A. Dolatshahi-Pirouz, *Adv. Mater.*, 2017, **29**, 1603612.

26 B. D. Kevadiya, G. V. Joshi, H. A. Patel, P. G. Ingole, H. M. Mody and H. C. Bajaj, *J. Biomater. Appl.*, 2010, **25**, 161–177.

27 P. Podsiadlo, A. K. Kaushik, E. M. Arruda, A. M. Waas, B. S. Shim, J. D. Xu, H. Nandivada, B. G. Pumplin, J. Lahann, A. Ramamoorthy and N. A. Kotov, *Science*, 2007, **318**, 80–83.

28 P. Ming, Z. F. Song, S. S. Gong, Y. Y. Zhang, J. L. Duan, Q. Zhang, L. Jiang and Q. F. Cheng, *J. Mater. Chem. A*, 2015, **3**, 21194–21200.

29 G. Huang, J. Xie, S. Shuai, S. Wei, Y. Chen, Z. Guan, Q. Zheng, P. Yue and C. Wang, *Int. J. Pharm.*, 2021, **594**, 120182.

30 J. Gao, M. R. Scheenstra, A. van Dijk, E. J. A. Veldhuizen and H. P. Haagsman, *Vet. Immunol. Immunopathol.*, 2018, **200**, 7–15.

31 Y. Zou, J. Zhang, J. Xu, L. Fu, Y. Xu, X. Wang, Z. Li, L. Zhu, H. Sun, H. Zheng and J. Guo, *Cell Biosci.*, 2021, **11**, 210.

32 J. Wu, A. Chen, Y. Zhou, S. Zheng, Y. Yang, Y. An, K. Xu, H. He, J. Kang, J. A. Luckanagul, M. Xian, J. Xiao and Q. Wang, *Biomaterials*, 2019, **222**, 119398.

33 S. Q. Nagelkerke, G. Dekkers, I. Kustiawan, F. S. van de Bovenkamp, J. Geissler, R. Plomp, M. Wuhrer, G. Vidarsson, T. Rispens, T. K. van den Berg and T. W. Kuijpers, *Blood*, 2014, **124**, 3709–3718.

34 T. Roszer, *Mediators Inflammation*, 2015, **2015**, 1–16.

35 M. H. Abdelaziz, S. F. Abdelwahab, J. Wan, W. Cai, H. Wang, J. Cheng, K. D. Kumar, A. Vasudevan, A. Sadek, Z. Su, S. Wang and H. Xu, *J. Transl. Med.*, 2020, **18**, 58.

36 E. Chen, G. Liu, X. Zhou, W. Zhang, C. Wang, D. Hu, D. Xue and Z. Pan, *FASEB J.*, 2018, **32**, 4917–4929.

37 K. Maciaszek, D. M. Brown and V. Stone, *Toxicol. In Vitro*, 2022, **78**, 105273.

38 M. Mori, R. Asahi, Y. Yamamoto, T. Mashiko, K. Yoshizumi, N. Saito, T. Shirado, Y. Wu and K. Yoshimura, *Mar. Drugs*, 2020, **18**, 520.

39 G. Orive, A. M. Carcaboso, R. M. Hernandez, A. R. Gascon and J. L. Pedraz, *Biomacromolecules*, 2005, **6**, 927–931.

40 E. H. Son, E. Y. Moon, D. K. Rhee and S. Pyo, *Int. Immunopharmacol.*, 2001, **1**, 147–154.

41 U. Galili, *Tissue Eng., Part B*, 2015, **21**, 231–241.

42 D. P. Vasconcelos, M. Costa, I. F. Amaral, M. A. Barbosa, A. P. Aguas and J. N. Barbosa, *Biomaterials*, 2015, **53**, 566–573.

43 P. H. Wooley, R. Morren, J. Andary, S. A. Sud, S. Y. Yang, L. Mayton, D. Markel, A. Sieving and S. Nasser, *Biomaterials*, 2002, **23**, 517–526.

44 K. A. Hooper, T. L. Nickolas, E. J. Yurkow, J. Kohn and D. L. Laskin, *J. Biomed. Mater. Res.*, 2000, **50**, 365–374.

45 G. C. Gurtner, S. Werner, Y. Barrandon and M. T. Longaker, *Nature*, 2008, **453**, 314–321.

46 O. Veiseh and A. J. Vegas, *Adv. Drug Delivery Rev.*, 2019, **144**, 148–161.

47 B. S. Guerrouahen, H. Sidahmed, A. Al Sulaiti, M. Al Khulaifi and C. Cugno, *Stem Cells Int.*, 2019, **2019**, 1–11.

48 Y. Zhu, H. Liang, X. Liu, J. Wu, C. Yang, T. M. Wong, K. Y. H. Kwan, K. M. C. Cheung, S. Wu and K. W. K. Yeung, *Sci. Adv.*, 2021, **7**, eabf6654.

49 D. M. Yu, B. Li, M. Yu, S. Guo, Z. Guo and Y. Han, *Bioact. Mater.*, 2022, **18**, 72–90.

50 J. Loeffler, F. A. Sass, S. Filter, A. Rose, A. Ellinghaus, G. N. Duda and A. Dienelt, *Front. Immunol.*, 2019, **10**, 2443.

51 P. L. Graney, S. Ben-Shaul, S. Landau, A. Bajpai, B. Singh, J. Eager, A. Cohen, S. Levenberg and K. L. Spiller, *Sci. Adv.*, 2020, **6**, eaay6391.

52 B. Bragdon, O. Moseychuk, S. Saldanha, D. King, J. Julian and A. Nohe, *Cell. Signalling*, 2011, **23**, 609–620.

53 G. Chen, C. Deng and Y.-P. Li, *Int. J. Biol. Sci.*, 2012, **8**, 272–288.

This journal is © The Royal Society of Chemistry 2023

J. Mater. Chem. B, 2023, **11**, 9933–9949 | **9949**